The Astronomical Journal, 147:15 (11pp), 2014 January doi:10.1088/0004-6256/147/1/15

THE UNEXPECTEDLY BRIGHT COMET C/2012 F6 (LEMMON) UNVEILED AT NEAR-INFRARED WAVELENGTHS*

Lucas Paganini[1,2], Michael A. DiSanti[1], Michael J. Mumma[1], Geronimo L. Villanueva[1,2], Boncho P. Bonev[1,2], Jacqueline V. Keane[3], Erika L. Gibb[4], Hermann Boehnhardt[5], and Karen J. Meech[3]
[1] Goddard Center for Astrobiology, NASA GSFC, MS 690, Greenbelt, MD 20771, USA; lucas.paganini@nasa.gov
[2] Department of Physics, Catholic University of America, Washington, DC 20064, USA
[3] Institute for Astronomy, University of Hawaii, Honolulu, HI 96822, USA
[4] Department of Physics & Astronomy, University of Missouri, St. Louis, MO 63121, USA
[5] Max-Planck-Institut für Sonnensystemforschung, D-37191, Katlenburg-Lindau, Germany
Received 2013 September 24; accepted 2013 October 25; published 2013 December 6

ABSTRACT

We acquired near-infrared spectra of the Oort cloud comet C/2012 F6 (Lemmon) at three different heliocentric distances (R_h) during the comet's 2013 perihelion passage, providing a comprehensive measure of the outgassing behavior of parent volatiles and cosmogonic indicators. Our observations were performed pre-perihelion at R_h = 1.2 AU with CRIRES (on 2013 February 2 and 4), and post-perihelion at R_h = 0.75 AU with CSHELL (on March 31 and April 1) and R_h = 1.74 AU with NIRSPEC (on June 20). We detected 10 volatile species (H_2O, OH^* prompt emission, C_2H_6, CH_3OH, H_2CO, HCN, CO, CH_4, NH_3, and NH_2), and obtained upper limits for two others (C_2H_2 and HDO). One-dimensional spatial profiles displayed different distributions for some volatiles, confirming either the existence of polar and apolar ices, or of chemically distinct active vents in the nucleus. The ortho–para ratio for water was 3.31 ± 0.33 (weighted mean of CRIRES and NIRSPEC results), implying a spin temperature >37 K at the 95% confidence limit. Our (3σ) upper limit for HDO corresponds to D/H < 2.45 × 10^{-3} (i.e., <16 Vienna Standard Mean Ocean Water, VSMOW). At R_h = 1.2 AU (CRIRES), the production rate for water was $Q(H_2O)$ = 1.9 ± 0.1 × 10^{29} s^{-1} and its rotational temperature was T_{rot} ∼ 69 K. At R_h = 0.75 AU (CSHELL), we measured $Q(H_2O)$ = 4.6 ± 0.6 × 10^{29} s^{-1} and T_{rot} = 80 K on March 31, and 6.6 ± 0.9 × 10^{29} s^{-1} and T_{rot} = 100 K on April 1. At R_h = 1.74 AU (NIRSPEC), we obtained $Q(H_2O)$ = 1.1 ± 0.1 × 10^{29} s^{-1} and T_{rot} ∼ 50 K. The measured volatile abundance ratios classify comet C/2012 F6 as rather depleted in C_2H_6 and CH_3OH, while HCN, CH_4, and CO displayed abundances close to their median values found among comets. H_2CO was the only volatile showing a relative enhancement. The relative paucity of C_2H_6 and CH_3OH (with respect to H_2O) suggests formation within warm regions of the nebula. However, the normal abundance of HCN and hypervolatiles CH_4 and CO, and the enhancement of H_2CO, may indicate a possible heterogeneous nucleus of comet C/2012 F6 (Lemmon), possibly as a result of radial mixing within the protoplanetary disk.

Key words: astrochemistry – comets: general – comets: individual (C/2012 F6 (Lemmon)) – molecular processes – Oort Cloud – planets and satellites: formation

Online-only material: color figures

1. INTRODUCTION

Comets visit the inner solar system from at least two long-term reservoirs—the scattered disk/Kuiper Belt (KB) and the Oort cloud (OC). But they actually agglomerated in other regions during the formative phase of the solar system. Indeed, icy bodies (such as comets and trans-Neptunian objects) are believed to preserve material from that time. While some may have experienced subsequent processing owing to the effects of thermal warming, exposure to energetic radiation, and/or collisions since their formation, the relatively pristine composition of others may reveal the physicochemical conditions that prevailed 4.6 billion years ago.

Although an ongoing subject of discussion, current evidence suggests that most comets might have formed in an extensive region near or around the CO_2 and CO snow lines (over the range in heliocentric distance R_h ∼ 5–30 AU; Dodson-Robinson et al. 2009; A'Hearn et al. 2012; Qi et al. 2013) before migrating to their current reservoirs (OC and KB; e.g., Gomes et al. 2005; Brasser & Morbidelli 2013). Further lines of evidence also suggest that a stationary formation (i.e., one not accounting for radial mixing) might not fully account for the diversity of volatile abundances and other cosmogonic parameters in icy bodies, such as spin temperatures and isotopic ratios (see Paganini et al. 2012, 2013a, and references therein). Indeed, prior to outward migration, small bodies could have experienced possible chemical processing as a result of dynamical translation within the disk driven by the inward and outward migration of Jupiter and Saturn in the first 100,000 yr after formation of the Sun (the so-called Grand Tack event; cf. Walsh et al. 2011 and references therein).

Thus far, the analysis of primary volatiles in cometary comae, i.e., species directly released from the nucleus (traditionally termed *parent species*), represents unique evidence for (relatively) unaltered material. The importance of such measurements is twofold: it might help us unveil the primordial conditions that occurred during the early solar system, and it might help us prove whether dynamical conditions played an important role during planetary formation. In addition to studies of product species at optical wavelengths (e.g., A'Hearn et al. 1995; Fink

* Based on observations obtained at the European Southern Observatory at Cerro Paranal, Chile, under program 290.C-5016, at the NASA's Infrared Telescope Facility, program 2013A_071, and Keck Observatory, program H233NS, at Mauna Kea, Hawaii.

Table 1
Log of the Observations

Instrument	Date (UT 2013)	R_h (AU)	Δ (AU)	Δ-dot (km s^{-1})	P.A. (°)	α (°)	Settings (Time on Source [minutes])
CRIRES	Feb. 2 07:28–09:32	1.20	0.99	−4	262.4	53.4	HCN(32), CH_3OH(12), CH(20)
CRIRES	Feb. 4 05:25–06:40	1.18	0.99	−2	287.6	52.3	H_2O(20), HDO(24)
CSHELL	Mar. 31 (Apr. 1) 19:45–(00:28)	0.75	1.55	+16	199.3	32.4	CO(12), C_2H_6(12), H_2O(32), CH_4(40), H_2CO(32)
CSHELL	Apr. 1(Apr. 2) 19:46–(01:08)	0.75	1.56	+15	201.8	31.8	C_2H_6(16), CH_3OH(26), H_2O(32), CO(12)
NIRSPEC	Jun. 20 12:04–15:18	1.74	1.79	+5	256.3	33.4	KL1(40), KL2(76)[a]

Notes. R_h: heliocentric distance; Δ: geocentric distance; Δ-dot: geocentric velocity; P.A.: position angle of the extended Sun–comet vector; α: solar phase (Sun–comet–Earth) angle. (These values represent the midpoint of data acquisition.)
[a] Both in KL1 and KL2 we targeted H_2O, C_2H_6, and CH_3OH, while KL2 also allowed estimates of H_2CO, HCN, NH_3, NH_2, and C_2H_2.

2009; Schleicher & Bair 2010; Langland-Shula & Smith 2011; Cochran et al. 2012), radio and infrared surveys of primary volatiles seek to build taxonomical databases for comets (for reviews, see Bockelée-Morvan et al. 2004; Mumma & Charnley 2011). Most of these studies show compositional diversity amongst objects from the OC and KB, thus demonstrating the need for more comprehensive statistical evaluations. Aided by dynamical (theoretical) studies and sample analyses of solid material (e.g., of returned dust samples; Brownlee et al. 2006), our ongoing IR survey is providing clues into the possible origins of the early solar system by analyzing a growing database of comets from both the OC and KB.

On 2012 March 23, Alex Gibbs of the Mount Lemmon Survey discovered an inbound faint object with a visual magnitude of ∼20 at 5 AU from the Sun, which subsequently was designated C/2012 F6 (Lemmon; hereafter C/2012 F6). Its eccentricity ($e = 0.998$), original semimajor axis[6] ($a = 458.08$ AU), Tisserand parameter ($T_j = 0.147$), and inclination to the ecliptic ($i = 82.^\circ6$) classify it as belonging to the nearly isotropic (long-period) comet group originating from the OC (Nakano 2013). In January 2013, the comet underwent significant brightening. This prompted several optical observations, which revealed a greenish coma, indicative of a volatile-dominated spectrum (e.g., atomic oxygen and various carbon- and nitrogen-bearing species). We initiated a worldwide campaign using different facilities, including VLT/CRIRES, Keck-2/NIRSPEC, and IRTF/CSHELL, in the infrared. Here, we present results obtained for several volatiles in C/2012 F6 during this campaign, including production rates, rotational temperatures, spatial profiles, and cosmogonic parameters (ortho–para ratio and D/H in water).

2. OBSERVATIONS AND DATA ANALYSIS

We obtained high-resolution near-IR spectra of comet C/2012 F6 on five dates spanning February through June 2013 (bracketing perihelion, $q = 0.73$ AU on 2013 March 24), using three separate spectrometer–telescope combinations. Table 1 presents a log of our observations.

With CRIRES we used the 0.″4 slit, which delivers high spectral resolving power ($\lambda/\Delta\lambda \sim 50{,}000$) and spatial coverage of 40″. The adaptive optics module (Multi-Applications Curvature Adaptive Optics) provided seeing correction and image stabilization, thereby delivering excellent spatial registration. On both nights, we oriented the slit at position angle 290°, i.e., close to the Sun–comet direction (262° on February 2 and 288° on February 4). Atmospheric conditions were stable on both nights: relative humidity was ∼20%, wind speeds were below 7 m s^{-1}, and seeing was in the range of 1.″0–1.″5. Standard star HR 5336 (located near the comet's trajectory) allowed flux calibration and measures of column content of absorbing species in the terrestrial atmosphere.

With CSHELL we used the 2″ wide slit, maximizing the flux collection while still delivering moderate resolving power ($\lambda/\Delta\lambda \sim 20{,}000$), which was adequate for our molecular studies. This slit width was necessary because C/2012 F6 was positioned 20°–25° south of the Sun and so was available only during daytime, which precluded use of the CCD guider in CSHELL. The 30″ long slit was oriented north–south on March 31, close to the projected Sun–comet direction (position angle 199°; Table 1), and east–west on April 1. Flux levels the terrestrial contribution were established through observations of the standard star HR 8728. For our CSHELL observations, three distinct but related science investigations were awarded eight consecutive days (UT March 25 through April 1), totaling 64 hr of clock time. However, problems associated with weather, observatory hardware, and high winds restricted our available time to the last two dates, resulting in a total of approximately 10 hr of clock time on the comet. The lack of active guiding during daytime[7] also reduced the observing efficiency (e.g., see DiSanti et al. 2009 for details). Our measurement strategy balanced volatiles measured in all observing epochs (H_2O, C_2H_6, and CH_3OH) against those that were not measured with CRIRES or NIRSPEC (CO and CH_4), owing to inadequate Doppler shift on those dates. The resulting production rates and abundance ratios are listed in Table 2.

NIRSPEC is a cross-dispersed echelle grating spectrometer that samples a wide range of spectral orders with relatively high spectral resolving power. On June 20, we used a 0.″432 × 24″ slit configuration (delivering $\lambda/\Delta\lambda \sim 25{,}000$) for observations of the

[6] S. Nakano Note, NK 2452, http://www.oaa.gr.jp/~oaacs/nk/nk2452.htm

[7] This resulted in an observing efficiency of approximately 37% for our CSHELL observations, based on 214 minutes of total on-source integration time over the two dates (UT March 31 and April 1; see Table 1).

Table 2
Molecular Abundances for Volatiles in Comet C/2012 F6 (Lemmon)[a]

Species	Date (UT)	ν[b] (cm^{-1})	Lines[c]	T_{rot} (K)	Global Q[d] (10^{27} s^{-1})	Abundance (Relative %)
2013 Feb 2[e]						
[f] $R_h = 1.20$ AU; $\Delta = 0.99$ AU; Δ-dot $= -2$ km s^{-1}; P.A. $= 262.^\circ4$; $\alpha = 53.^\circ4$						
OH*	Feb 2.31	mult.	24	(70)	187.88 ± 27.56	99
CH_3OH	Feb 2.39	2840.61	10	66^{+11}_{-9}[g]	3.50 ± 0.47	1.85 ± 0.27
C_2H_6	Feb 2.35	2992.68	6	69^{+9}_{-7}	0.49 ± 0.06	0.26 ± 0.03
C_2H_2	Feb 2.35	3293.80	9	(70)	<0.10	<0.05
HCN	Feb 2.31	3299.52	3	(70)	0.21 ± 0.08	0.11 ± 0.05
H_2CO	Feb 2.31	2811.05	7	(70)	<0.22	<0.12
NH_2	Feb 2.31	3310.10	4	(70)	0.58 ± 0.13	0.31 ± 0.07
NH_3	Feb 2.31	3295.39	1	(70)	<1.20	<0.63
2013 Feb 4						
[f] $R_h = 1.18$ AU; $\Delta = 0.99$ AU; Δ-dot $= -4$ km s^{-1}; P.A. $= 287.^\circ6$; $\alpha = 52.^\circ3$						
H_2O	Feb 4.23	3014.67	8	69^{+8}_{-5}	189.05 ± 11.04	100
OH*	Feb 4.23	3397.83	3	(70)[g]	168.39 ± 14.98	89
HDO	Feb 4.25	2683.36	11	(70)	$<0.93 \pm 0.31$	<0.49
2013 Mar 31[h]						
[f] $R_h = 0.75$ AU; $\Delta = 1.55$ AU; Δ-dot $= +16$ km s^{-1}; P.A. $= 199.^\circ3$; $\alpha = 32.^\circ4$						
H_2O	Mar 31.86	mult.	6/15	80^{+10}_{-10}	459 ± 65	100
CO	Mar 31.82	2152.64	2	(80)	19.5 ± 2.2	4.25 ± 0.64
C_2H_6	Mar 31.85	2981.86	2	(80)	1.80 ± 0.24	0.39 ± 0.07
CH_3OH	Mar 31.85	2984.34	1	(80)	6.16 ± 0.68	1.34 ± 0.24
CH_4	Mar 31.93	3040.64	1	(80)	3.06 ± 0.57	0.67 ± 0.11
H_2CO	Mar 31.98	2783.60	3	(80)	2.46 ± 0.45	0.54 ± 0.12
2013 Apr 1[h]						
[f] $R_h = 0.75$ AU; $\Delta = 1.56$ AU; Δ-dot $= +15$ km s^{-1}; P.A. $= 201.^\circ8$; $\alpha = 31.^\circ8$						
H_2O	Apr 1.90	2984.34	6/8	100^{+10}_{-10}	661 ± 92	100
CO	Apr 2.03	2152.64	2	(100)	25.2 ± 2.3	3.82 ± 0.63
C_2H_6	Apr 1.81	2985.00	2	(100)	2.18 ± 0.22	0.33 ± 0.13
CH_3OH	Apr 1.84	mult.[e]	3	(100)	6.76 ± 0.51	1.02 ± 0.39
2013 Jun 20						
[f] $R_h = 1.74$ AU; $\Delta = 1.79$ AU; Δ-dot $= +5$ km s^{-1}; P.A. $= 256.^\circ3$; $\alpha = 33.^\circ4$						
H_2O	Jun 20.50	3441.46	11	50^{+7}_{-6}	105.4 ± 6.6	100
C_2H_6	Jun 20.50	2945.67	13	59^{+14}_{-10}	0.31 ± 0.03	0.29 ± 0.03
CH_3OH	Jun 20.50	2908.89	17	50^{+7}_{-5}	1.56 ± 0.14	1.48 ± 0.16
HCN	Jun 20.55	3299.54	5	(50)	0.23 ± 0.02	0.22 ± 0.03
NH_3	Jun 20.55	3295.42	1	(50)	0.64 ± 0.22	0.61 ± 0.21
NH_2	Jun 20.55	3301.84	2	(50)	0.12 ± 0.03	0.12 ± 0.03
C_2H_2	Jun 20.55	3295.94	8	(50)	<0.06	<0.06
H_2CO	Jun 20.55	2851.41	6	(50)	<0.25	<0.24

Notes.

[a] Uncertainties represent 1σ, and upper limits represent 3σ. The reported error in production rate includes the line-by-line scatter in measured column densities, along with photon noise, systematic uncertainty in the removal of the cometary continuum, and (minor) uncertainty in rotational temperature.

[b] Mean wavenumber of all emission lines (used for this reduction) from a particular species.

[c] "Lines" refers to the number of spectral intervals sampled. For the CSHELL water observations, the first entry indicates the number of intervals in the H2O_3A setting that were used to determine T_{rot}. The second entry indicates the total number of intervals used to calculate $Q(H_2O)$, including water lines in the H2O_3A and CO_K settings, and OH* in the CH4_E and H2CO_B settings on March 31 and in the CH3OH_A setting on April 1, as indicated in Table 1.

[d] Global production rate, after applying a measured growth factor of (1.7 ± 0.2) and (1.7 ± 0.1) to the nucleus-centered production rates of volatiles measured on UT 2013 February 2 and February 4, respectively. For CSHELL (March 31 and April 1), growth factors were: H_2O (2.0 ± 0.2), CO (1.9 ± 0.1), C_2H_6 (1.8 ± 0.05), CH_3OH (2.3 ± 0.1), CH_4 (2.2 ± 0.1), and H_2CO (1.8 ± 0.2). For NIRSPEC (June 20), GFs were: 3.1 ± 0.2 for H_2O and 1.8 ± 0.1 for minor species (based on measurements of C_2H_6, CH_3OH, and HCN).

[e] We adopt $Q(H_2O)$ from February 4, which is consistent with production rates from (mean) $Q(H_2O)$ and $Q(OH^*)$ from the combined CH, HCN, and CH_3OH settings on February 2.

[f] R_h: heliocentric distance; Δ: geocentric distance; Δ-dot: geocentric velocity; P.A.: position angle of the extended Sun–comet vector; α: solar phase (Sun–comet–Earth) angle for the midpoint of data acquisition.

[g] We adopted T_{rot} (shown in parentheses) based on values measured for C_2H_6, CH_3OH, and H_2O from CRIRES and NIRSPEC spectra, and for H_2O from CSHELL spectra when calculating the NC production rates for species whose T_{rot} determination was not possible.

[h] For trace species measured on both dates, we obtained the following weighted mean values, 10^{27} s^{-1} (%): C_2H_6: 2.0 ± 0.2 (0.38 ± 0.06), CH_3OH: 6.0 ± 0.4 (1.25 ± 0.20), CO: 2.2 ± 0.2 (4.03 ± 0.45).

Table 3
Summary of Molecular Abundances Ratios in Comet C/2012 F6 (Lemmon)

Species	Date (UT 2013)					Weighted Mean
	Feb 2	Feb 4	Mar 31	Apr 1	Jun 20	% ($H_2O = 100$)
C_2H_6	0.26 ± 0.03		0.39 ± 0.07	0.33 ± 0.13	0.29 ± 0.03	0.29 ± 0.02
CH_3OH	1.85 ± 0.27		1.34 ± 0.24	1.02 ± 0.39	1.48 ± 0.16	1.48 ± 0.11
HCN	0.11 ± 0.05				0.22 ± 0.03	0.19 ± 0.03
CO			4.25 ± 0.64	3.82 ± 0.63		4.03 ± 0.45
CH_4			0.67 ± 0.11			0.67 ± 0.11
H_2CO	<0.12		0.54 ± 0.12		<0.24	0.54 ± 0.12
NH_3	<0.63				0.61 ± 0.21	0.61 ± 0.21
NH_2	0.31 ± 0.07				0.12 ± 0.03	0.15 ± 0.03
C_2H_2	<0.05				<0.06	<0.05
HDO		<0.49				<0.49

comet, with the slit positioned along the projected Sun–comet direction. Flux calibration was achieved through observations of the IR standard star HR 6707 with a $0\farcs720 \times 24''$ slit configuration.

Comet spectra were acquired in our standard four-step sequence (ABBA), with accumulated times of 30, 60, or 120 s per stored A or B frame (depending on the instrument used and wavelengths targeted). In both the CRIRES and CSHELL cases, the telescope was nodded along the slit by $15''$ between the A and B positions, and with NIRSPEC the telescope was nodded by $12''$.

Data reduction and analysis of the spectral frames included flat fielding, removal of pixels affected by high dark current and/or cosmic-ray hits, spatial and spectral rectification, and spatial registration of individual A and B beams. After combining the A and B beams from the (processed) difference frames, which further assists in removing any residual background emission, we extracted spectra by summing 15 spatial pixels ($1\farcs3$) centered on the nucleus for the CRIRES observations, 10 pixels ($2\farcs0$) for the CSHELL observations, and 9 pixels ($1\farcs3$) for the NIRSPEC observations. We synthesized a transmittance function for the terrestrial atmosphere by fitting the absorptions observed in the standard star spectra, and adjusting the estimated atmospheric contribution until an optimum fit was obtained. We used a multiple layer atmosphere and the LBLRTM model (Clough et al. 2005) that accessed the HITRAN 2008 molecular database modified with our custom updates (see, e.g., Villanueva et al. 2011b for details). We convolved our synthetic transmittance function to the resolving power of the comet observations, scaled it to the cometary continuum, and subtracted it from the measured spectrum. This isolated the net emission spectrum in excess of the cometary continuum. We then generated a fully resolved transmittance function for use in extracting the true transmittance experienced by individual spectral lines at their Doppler-shifted wavelengths.

These observations allowed robust measures of pre-perihelion rotational temperatures and production rates for multiple species (Paganini et al. 2013b). The simultaneous measurement of H_2O and its direct proxy (OH^*) in each instrument setting permitted accurate characterization of the abundance ratio for each trace species. Spectra of H_2O and OH^* are shown in Figure 1, and of other primary volatiles in Figure 2. Spectra resulting from the HDO setting are shown in Figure 3, along with a synthetic spectrum of expected HDO lines. With CRIRES, six volatiles (H_2O, OH^*, C_2H_6, HCN, CH_3OH, and NH_2) were securely detected, and upper limits were retrieved for H_2CO, NH_3, C_2H_2, and HDO. Three of these species (H_2O, C_2H_6, and CH_3OH) were also measured with CSHELL and NIRSPEC. With CSHELL we also detected H_2CO, CO, and CH_4 on March 31/April 1 (Figure 4; DiSanti et al. 2013b). The latter two molecules require a geocentric velocity (Δ-dot) of $\sim$10 km s^{-1} or higher to displace comet lines from their (opaque) terrestrial counterparts (Figure 4). Comet C/2012 F6 presented small Doppler shifts during the CRIRES and NIRSPEC observations, preventing detection of CO and CH_4 (Table 1).

3. RESULTS

We determined the rotational temperature ($T_{\rm rot}$) for an individual species, and we use this to quantify the production rate from the measured line fluxes. Results are given in Table 2, and the abundances obtained during our entire observing campaign are summarized in Table 3. The detailed procedures are discussed below.

3.1. Rotational Temperatures

The rotational temperature is obtained for an individual species by comparing modeled and observed fluxes for lines that span a sufficient range of rotational energies. The modeled spectral line intensities are derived from our custom quantum mechanical fluorescence models, which provide fluorescence efficiencies (g-factors) at the specified rotational temperature. The test temperature is modified iteratively until a satisfactory fit is obtained, and that optimum value for $T_{\rm rot}$ (and its uncertainty) then permits a robust measure of production rate. The number of lines used for each species and the values retrieved for $T_{\rm rot}$ and its uncertainty are as follows. With CRIRES, we measured $T_{\rm rot} = 69^{+9}_{-7}$ K for ethane (6 emission lines) and 66^{+11}_{-9} K for methanol (10 lines) on February 2, and 69^{+8}_{-5} K for H_2O (8 lines) on February 4. With CSHELL, we obtained $T_{\rm rot} = 80 \pm 10$ K on March 31 and 100 ± 10 K on April 1, based on a setting containing six lines of H_2O. Observations with NIRSPEC on June 20 resulted in $T_{\rm rot} = 50^{+7}_{-6}$ K, 59^{+14}_{-10} K, and 50^{+7}_{-5} K for water (11 lines), ethane (13 lines), and methanol (17 lines), respectively. See also Table 2.

3.2. Production Rates and Molecular Abundances

Using the optimum value for $T_{\rm rot}$, an apparent production rate is determined from the flux of each rovibrational transition detected within our sampled aperture, $F_{\rm line}$ (W m^{-2}). Our methodology considers the molecular lifetime τ(s), the molecular fluorescence efficiency or g-factor (g_i) at the appropriate $T_{\rm rot}$ and heliocentric velocity (v), terrestrial transmittance (T_i), geocentric distance (Δ), and the fraction of the total molecular content in the coma sampled by each pixel $f(x)$.

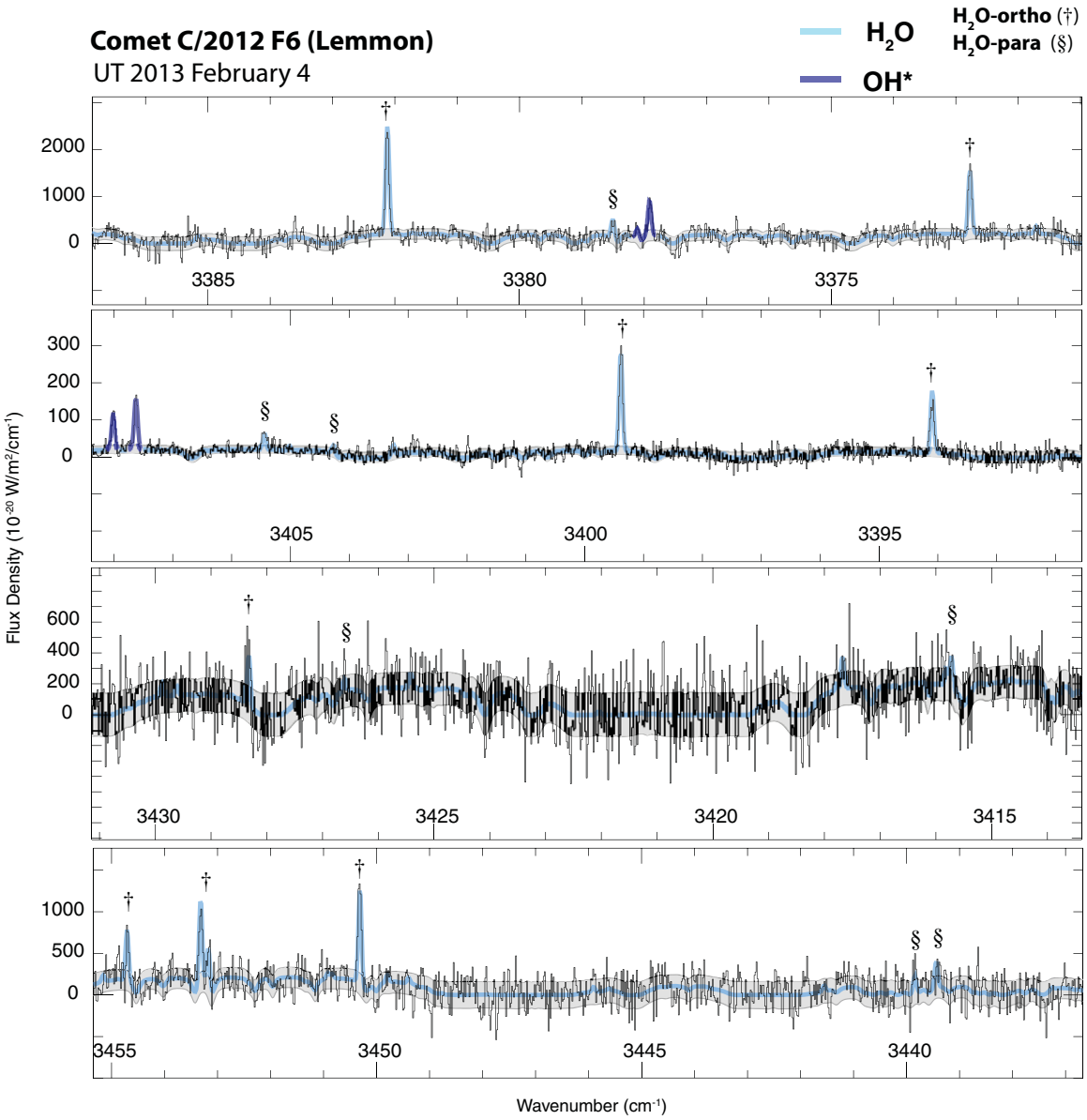

Figure 1. Water and OH prompt emission (OH*) lines detected in comet C/2012 F6 (Lemmon) on UT 2013 February 4. H_2O ortho and para emission lines are identified in the spectra. Here and in Figures 2 and 3, the gray region identifies the $\pm 1\sigma$ uncertainty, and the underlying colored lines depict the modeled spectra. (A color version of this figure is available in the online journal.)

The nucleus-centered production rate is calculated using

$$Q_{\rm nc} = \frac{4\pi\Delta^2 F_{\rm line}}{\tau g_i T_i f(x)}.$$

Our IR observations are impacted by slit losses (i.e., loss of flux) that result from atmospheric "seeing" and slight aperture effects (e.g., imperfect centering of the cometary photocenter in the slit). To correct for these effects, we obtain a growth factor (GF) from the observed spatial profiles after averaging Q at diametrically opposite positions along the slit, as this averages asymmetries in outflow (Xie & Mumma 1996). For our infrared observations, multiplying the $Q_{\rm nc}$ by GF results in total (or "global") production rates, $Q_{\rm tot}$.

Details of fluorescence models for each molecule can be found as follows: H_2O, HDO (Villanueva et al. 2012b), OH* (Bonev et al. 2006), C_2H_6 (Villanueva et al. 2011a), CO, C_2H_2, and CH_4 (Paganini et al. 2013a; Villanueva et al. 2011b; Gibb et al. 2003), NH_3, HCN (Villanueva et al. 2013; Lippi et al. 2013), NH_2 (Kawakita & Mumma 2011), H_2CO (DiSanti et al. 2006), and CH_3OH (Villanueva et al. 2012a; DiSanti et al. 2013a).

Obtaining reliable spatial profiles for observed volatiles requires adequate signal-to-noise ratios. CRIRES achieved such profiles for H_2O and C_2H_6, and for the continuum (see Figure 5(A)). These spatial profiles (pre-perihelion) reveal a fairly symmetric distribution of outgassing around the nucleus out to projected distances near 2000 km (as projected onto the sky plane), with some excess in the range ~1000–1500 km, perhaps indicating the presence of icy grains toward the northwest (i.e., relative anti-sunward direction).

With CSHELL (Figure 5(B)), we obtained spatial profiles for H_2O, C_2H_6, CO, and H_2CO. Compared to profiles obtained with CRIRES, the spatial distribution of H_2O, C_2H_6, CO, and the continuum extended to significantly larger nucleocentric distances (to ~4000 km), owing to the larger production rates at

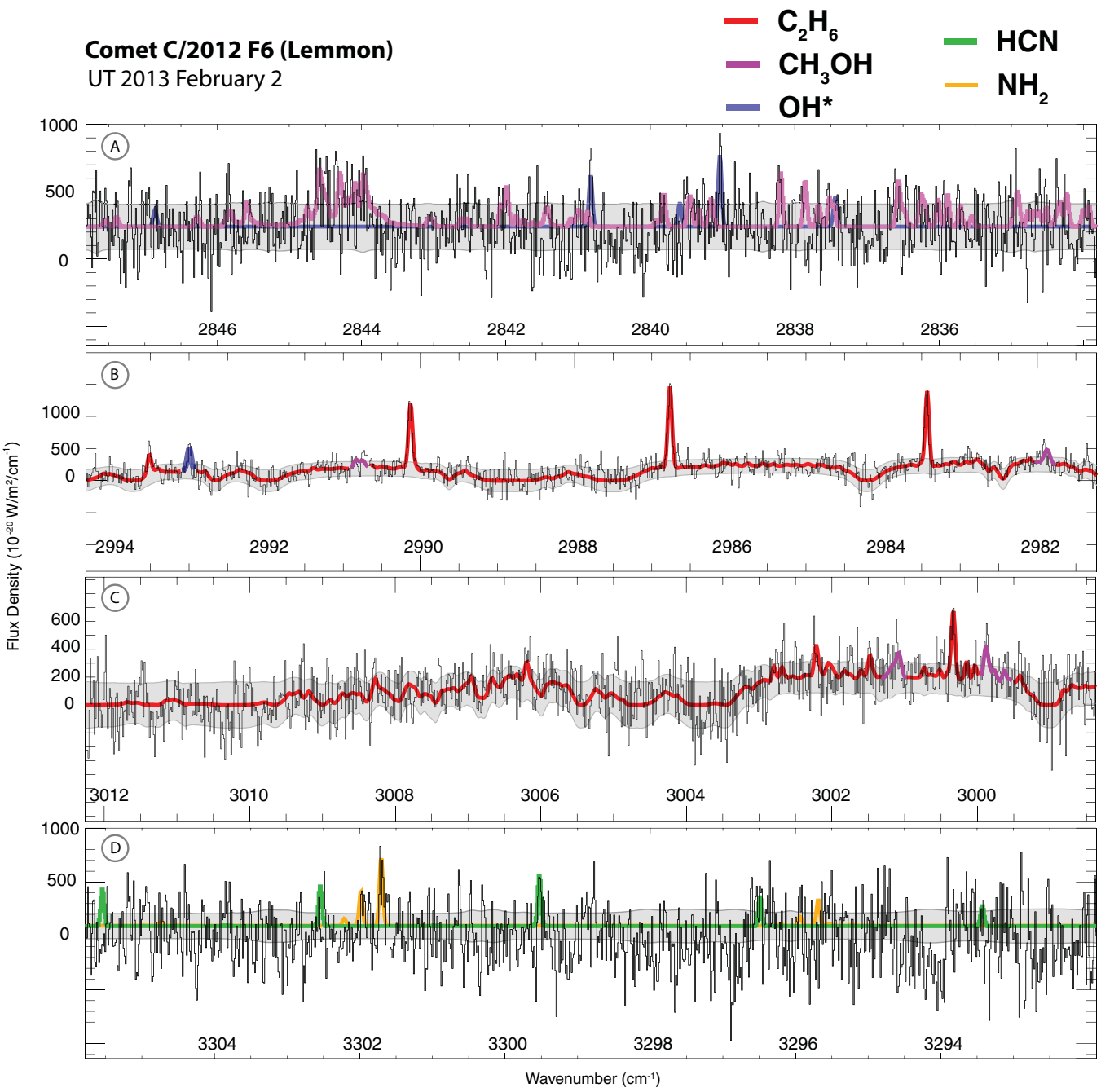

Figure 2. CRIRES observations of minor volatiles on UT 2013 February 2. Panel (A) displays the methanol ν_3 band and several OH* emission lines. Panels (B) and (C) show the 2982–3012 cm^{-1} range covering the ethane ν_7 band (P, R, and Q lines) along with a line of OH* and several emission lines of methanol. Panel (D) shows HCN emission lines with radical NH_2.

(A color version of this figure is available in the online journal.)

0.75 AU versus 1.2 AU (with CRIRES). Formaldehyde extended to ~3500 km and displayed stronger intensities toward the anti-sunward direction. The continuum showed a rather symmetric distribution about the nucleus, while CO was enhanced in the sunward direction and C_2H_6 showed some excess flux in the anti-sunward direction. In agreement with CRIRES, the H_2O profile is rather symmetric with some enhancement in the anti-sunward direction at about 2000 km, similar to C_2H_6. The different configurations of CO, H_2O, and C_2H_6 could be related to separate polar and apolar release of ices in the nucleus (see Section 4.3). NIRSPEC profiles also revealed enhancement of C_2H_6 in the anti-sunward direction (similar to HCN and H_2O; Figure 5(C)). On the other hand, methanol shows a rather symmetric distribution about the nucleus, and the continuum was stronger in the sunward direction. The observed (flux) enhancement of H_2O relative to other minor volatiles could be related to the release of icy grains at $R_h = 1.78$ AU.

3.2.1. CRIRES Observations

The production rates and mixing ratios for water and seven trace species are given in Table 2. Our value for water production on February 4 ($Q_{tot} = 1.9 \pm 0.1 \times 10^{29}$ molecules s^{-1}) agrees with estimates of H_2O production using OH prompt emission lines (OH*, a direct proxy for water) detected in the CH, CH_3OH, and HCN settings on February 2, and in the HDO

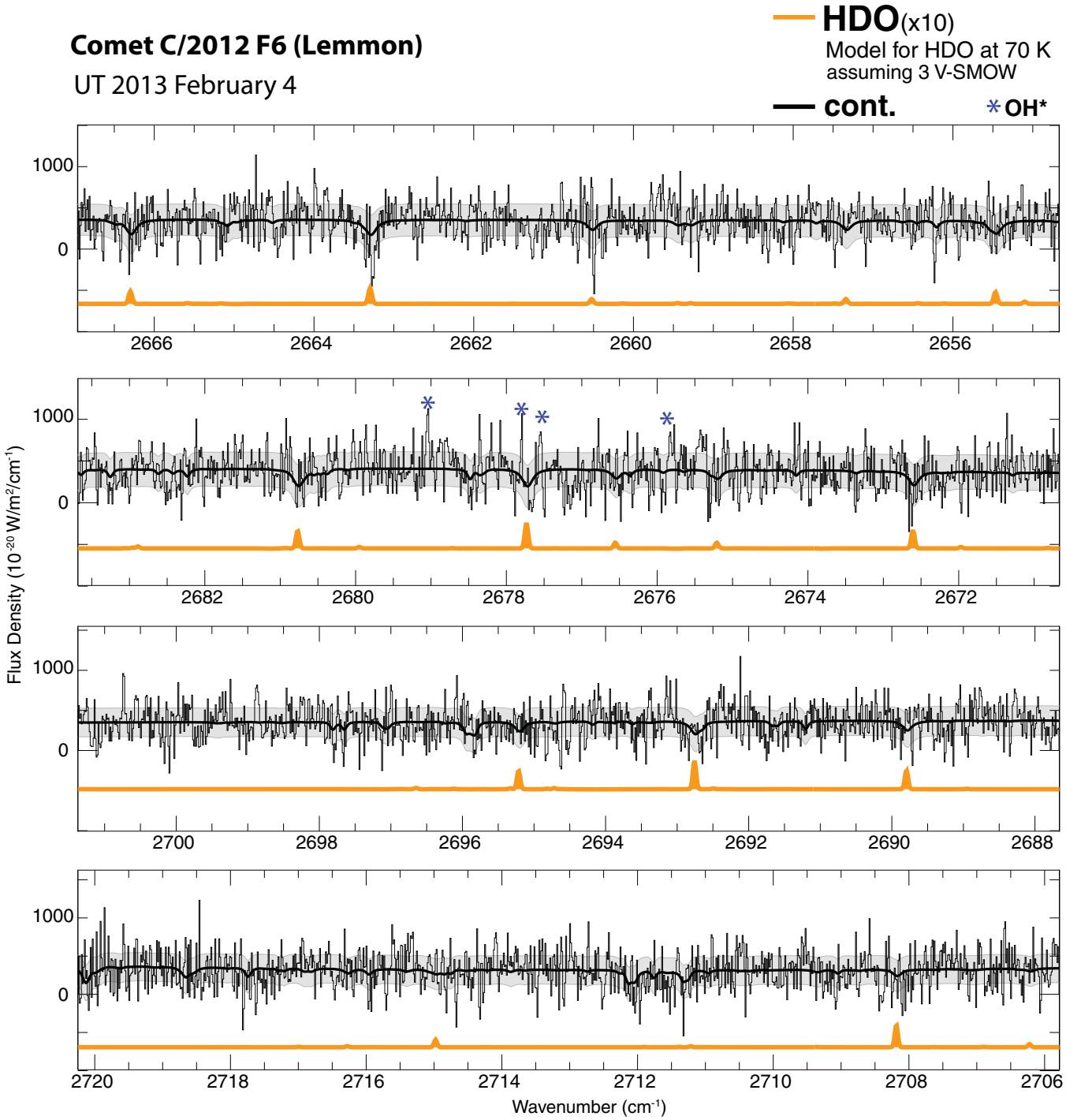

Figure 3. Spectra resulting from the CRIRES HDO setting. Observations of HDO were strongly affected by terrestrial extinction due to the low geocentric velocity of C/2012 F6 on February 4 (-2 km s^{-1}), and this limited our sensitivity.

(A color version of this figure is available in the online journal.)

and H_2O settings on February 4 (Table 2). Our results show no evidence for *significant* variation in water production on February 2 and 4; we therefore conclude that adopting this value for both nights provides an accurate measure of molecular abundances.

3.2.2. CSHELL Observations

CSHELL observations occurred shortly after perihelion, when the gas production was larger than when measured pre-perihelion with CRIRES. The water production rate on April 1 ($6.6 \pm 0.9 \times 10^{29}$ s^{-1}) was marginally higher than on March 31 ($4.6 \pm 0.6 \times 10^{29}$ s^{-1}), an increase by a factor of 1.5 ± 0.4, or $\sim 1.5\sigma$ based on their combined uncertainties. The production rates for C_2H_6, CH_3OH, and CO were also somewhat higher on April 1, but the abundance ratios for trace gases were systematically lower on April 1 than on March 31 (see Table 2). However, both quantities were unchanged within their 1σ uncertainties, even though the slit was oriented north–south on March 31 and east–west on April 1 (see Table 2). This

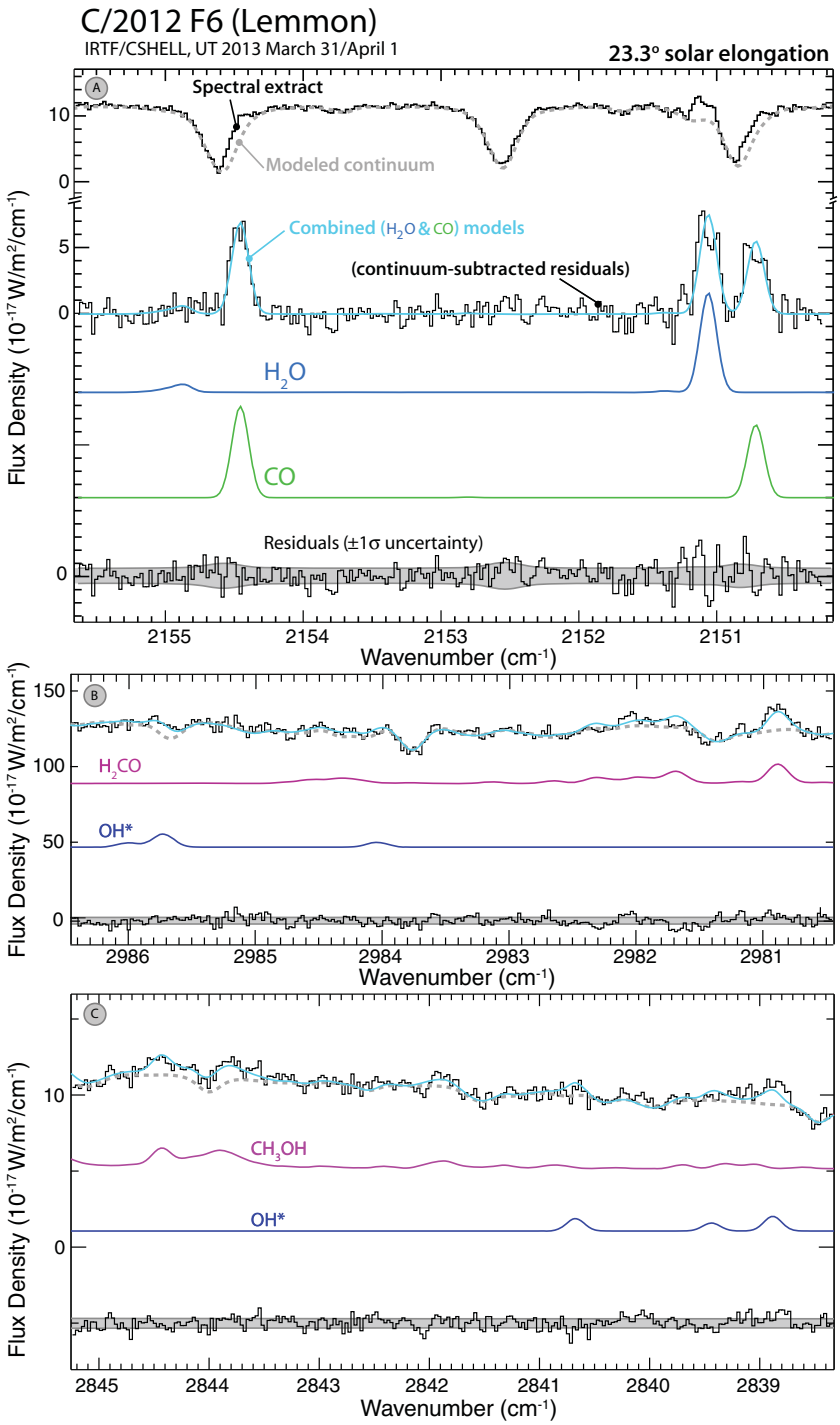

Figure 4. Example of volatiles detected with CSHELL along with model fits of the cometary continuum (dashed lines) to extract emission spectra. Our fluorescence models of these spectra allow us to obtain production rates for these species. Panel (A) shows the 2150–2156 cm^{-1} range, in which the continuum-subtracted residuals contain the emission lines of H_2O and CO. Similarly, panels (B) and (C) show detections of H_2CO, CH_3OH (Q branch), and OH^*.

(A color version of this figure is available in the online journal.)

suggests a non-varying composition for the responsible source region(s).

3.2.3. NIRSPEC Observations

Our observing campaign concluded with a run on June 20, when comet C/2012 F6 was at 1.74 AU from the Sun and 1.79 AU from Earth. The water production rate was $1.1 \pm 0.1 \times 10^{29}$ s^{-1}, and we securely detected C_2H_6, CH_3OH, HCN, NH_3, and NH_2. The results are listed in Table 2.

4. DISCUSSION

4.1. Water Production

The H_2O production rates we measured with CRIRES and CSHELL follow a heliocentric power law of $R_h^{-2.2 \pm 0.8}$, which is consistent with insolation-limited outgassing, while a comparison of CSHELL and NIRSPEC observations resulted in a power law of $R_h^{-1.9 \pm 0.4}$. A possible explanation for the relative increase in water production between March 31 and April 1 is

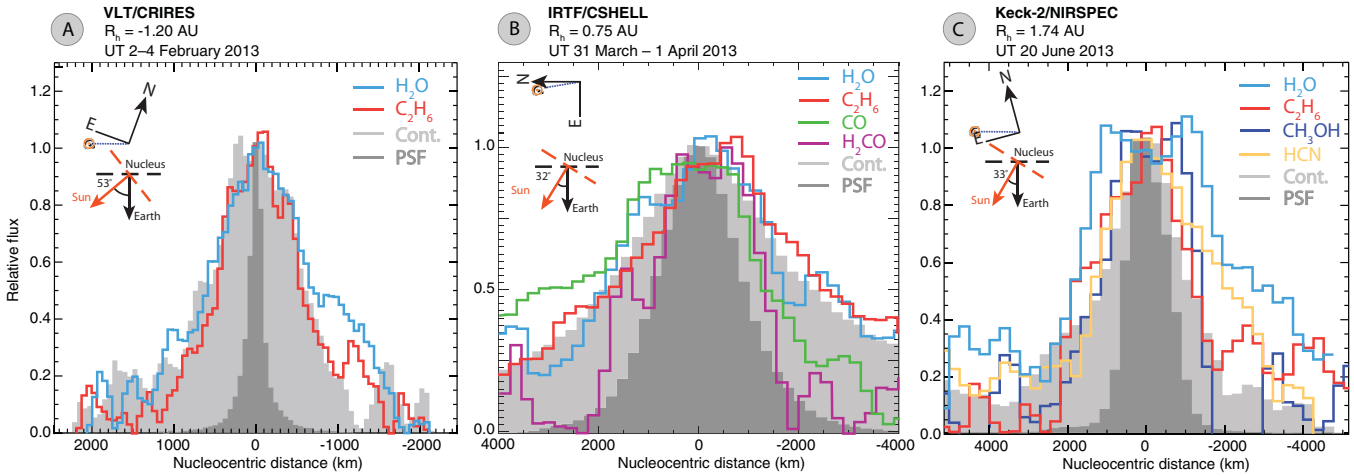

Figure 5. One-dimensional spatial profiles of primary volatiles and the continuum during the inbound (A: CRIRES) and outbound (B: CSHELL, C: NIRPSEC) passage of comet C/2012 F6 (Lemmon). The cardinal directions (i.e., the Sun–comet vector and solar phase angle) are indicated relative to the slit orientation, which is horizontal with respect to these plots. For further details, see Section 3.2.

(A color version of this figure is available in the online journal.)

the presence of strong jets near perihelion; however, in this case we would expect pronounced asymmetries that are not seen in our H_2O profiles (Figure 5). The most straightforward explanation favors an increase in overall gas production on April 1, perhaps due to preferential exposure of a larger or more active vent as a result of nucleus rotation, although the limited data sample restricts any conclusive interpretation.

In Figure 6, we compare our measured H_2O production rates with those inferred from Lyα using the SWAN all-sky camera on the *Solar and Heliospheric Observatory* (*SOHO*; Combi et al. 2013), and preliminary results inferred from the optical OH using the TRAPPIST telescope (revised estimates; Opitom et al. 2013a, 2013b; C. Opitom 2013, private communication). We do observe a systematic difference between the TRAPPIST results (from measurements of OH using $Q(H_2O) = 1.1\ Q(OH)$) and those obtained with other techniques.

We also compare with $Q(H_2O)$ estimated from visual magnitudes from Seiichi Yoshida's webpage[8] using the empirical relation $\log Q(H_2O) = 30.675 - 0.2453(m_v - 5 \log \Delta)$ given by Jorda et al. (2008). In early February, all three techniques (CRIRES, SWAN, and empirical estimates) provided similar results. However, the Jorda relation should be used with caution, since it does not account for the large differences seen among comets in C_2 emission intensities, in grain size distributions, and also in dust/gas ratios, all of which can influence the visible magnitude and thus introduce significant systematic uncertainties. Bearing in mind these limitations, these optical magnitudes provide estimates of $Q(H_2O)$ in the range of 1.2–2.2 $\times$ 10^{29} s^{-1}, consistent with *SOHO*/SWAN values (1.6–2.1 $\times$ 10^{29} s^{-1}) and also with our CRIRES value (1.9 $\pm$ 0.1 $\times$ 10^{29} s^{-1}).

Our CSHELL production rate for H_2O on March 31 (4.6 $\pm$ 0.6 $\times$ 10^{29} s^{-1}) is lower than the prediction based on the Jorda estimate ($\sim$(6.2–11.2)$\times 10^{29}$ s^{-1}); however, our value on April 1 (6.6 $\pm$ 0.9 $\times$ 10^{29} s^{-1}) is consistent with the predicted value at the 1σ level. The SWAN values show better agreement with the predicted estimates. However, although each SWAN measurement represents the mean water production averaged over $\sim$10 days, the day-to-day variations near perihelion exhibit significant excursions—relatively larger than the (marginal) increase we measured between March 31 and April 1. Similar variations are not seen in the SWAN results in early February, around the time of our CRIRES observations. This could point to substantially more variable gas production around perihelion.

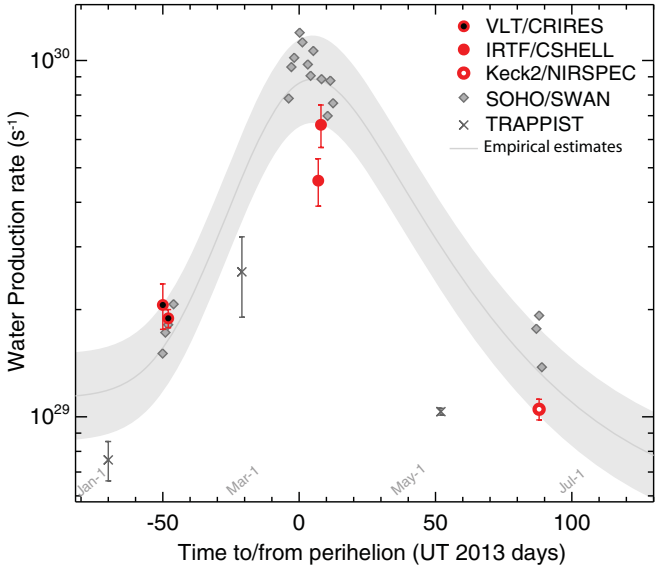

Figure 6. Comparison of measured and estimated H_2O production rates: IR facilities VLT/CRIRES, IRTF/CSHELL, and Keck2/NIRSPEC; the SWAN all-sky Lyα camera on the Solar and Heliospheric Observatory (Combi et al. 2013); the TRAPPIST telescope (revised estimates; Opitom et al. 2013a, 2013b; C. Opitom 2013, private communication); and empirical estimates. The latter estimates represent only first-order approximations of $Q(H_2O)$ derived from visual magnitudes (m_v) at optical wavelengths and the empirical relation of Jorda et al. (2008), $\log Q(H_2O) = 30.675 - 0.2453(m_v - 5 \log \Delta)$. For m_v we used Yoshida's estimates based on optical observations($m_v = 5.2 + 10 \log R_h$); see http://www.aerith.net/comet/catalog/2012F6/2012F6.html. We arbitrarily include an uncertainty $\sigma m_v \pm 0.5$, displayed as the shaded gray region. These estimates are subject to certain uncertainties discussed in Section 4.1; however, the shape of the curve (variation with heliocentric distance) is less subject to such variations.

(A color version of this figure is available in the online journal.)

The water production rate we obtained with NIRSPEC (1.1 $\pm$ 0.1 $\times$ 10^{29} s^{-1}) on June 20 ($R_h = 1.74$ AU) allows us to quantify a rather comprehensive evolution pre- and post-perihelion of comet C/2012 F6. At the 2σ level, our measurements display a behavior similar to estimates derived from the *SOHO*/SWAN

[8] http://www.aerith.net/comet/catalog/2012F6/2012F6.html

results and the Jorda approximation. Even though our IR observations provide a general overview of the overall evolution of water production and abundance of minor volatiles (relative to water), upcoming measurements from other facilities will add key information to the evolution of water production rates, and thus the real behavior of comet C/2012 F6.

4.2. Abundances of Trace Volatiles—Placing C/2012 F6 (Lemmon) in Context

Our water production rates on March 31 and April 1 were a factor of ∼2–3 higher than on February 4, which is reasonable considering the difference in R_h (Table 1). The observed decrease between March 31/April 1 and June 20 is likewise consistent with increasing heliocentric distance. For a homogeneous volatile composition, the abundance ratios of minor volatiles relative to H_2O are expected to be independent of heliocentric distance—at least within the regime of H_2O-driven activity encompassing our observations.

We observed only two minor volatiles (C_2H_6 and CH_3OH) in all three observing runs (Tables 1–3). The abundance ratios for C_2H_6 and CH_3OH relative to H_2O on February 2 agree (within 1.5σ) with their corresponding values on March 31 and April 1, and also (within 1σ) with values on June 20, suggesting consistent relative production of these (key) species pre- and post-perihelion.

Based on the weighted mean abundances (Table 3), our observations show that C_2H_6 in C/2012 F6 is depleted by approximately a factor of two relative to that measured in the majority of OC comets (i.e., relative to the current "normal" value; see Mumma & Charnley 2011), and similarly for CH_3OH (typical "normal" values for C_2H_6 and CH_3OH are ∼0.5% and ∼2%–3%, respectively). Our measured abundance of CO is consistent with its median value found among comets (∼4%), HCN is consistent with its "normal" abundance (∼0.2%), CH_4 is slightly below its median value (0.9%–1%), and H_2CO is above the values found for (native) formaldehyde in a number of comets measured to date (typically ∼0.1%–0.2%) and is closer to the higher abundances (>0.5%) seen in C/2002 T7 (LINEAR), C/2002 C1 (Ikeya-Zhang), and 9P/Tempel 1 (DiSanti et al. 2002, 2006; Mumma et al. 2005).

4.3. Possible Interpretation of Chemical Abundances in C/2012 F6

The observed depletion of some volatiles in this comet could indicate formation in, or a possible (later) exposure to, warm environments, whose temperatures were high enough to produce subsequent redistribution of these volatiles within (or escape from) the nucleus. However, the normal abundance of HCN, CH_4, and CO, plus the enhancement of formaldehyde (believed to have formed beyond the CO snow line via H-atom addition to CO-rich ices; Tielens & Hagen 1982), argues against formation under such conditions and suggests possible heterogeneity in this comet. The latter suggests that either (1) there was radial mixing during the formation of this icy body, (2) some volatiles were selectively shielded in water ice mantles during accretion, or (3) that the nucleus is composed of different structural phases of ice (polar and apolar), as, for instance, observed recently in comets C/2007 W1 (Boattini), 103P/Hartley 2, and C/2009 P1 (Garradd; Villanueva et al. 2011a; Mumma et al. 2011; Paganini et al. 2012). Alternatively, post-processing in the protoplanetary disk (cf. the Grand Tack model) or in the cometary reservoirs (OC/KB) should not be disregarded.

4.4. D/H in Water

Observations of HDO were adversely affected by terrestrial extinction due to the low geocentric velocity of C/2012 F6 on February 4 (-2 km s^{-1}), and this limited our sensitivity (Figure 3). Regardless of these limitations, we obtained an upper limit (3σ) for HDO of $<0.9 \times 10^{27}$ s^{-1}, corresponding to a D/H ratio in water of $<2.45 \times 10^{-3}$ (<16 VSMOW). Although not restrictive, this upper limit is consistent with values found in other comets (Mumma & Charnley 2011 and references therein; Hartogh et al. 2011; Bockelée-Morvan et al. 2012; Lis et al. 2013).

4.5. Ortho–Para Ratio in Water

If we assume that the ratio of nuclear spin species remains unaltered after incorporation in the cometary nucleus, the ortho–para ratio (OPR) of water should serve as an indicator of thermal conditions during its origins. A measurement of the OPR was obtained from water emission lines detected using CRIRES observations on February 2 and with NIRSPEC on June 20. Figure 1 shows the CRIRES detection of ortho- and para-water and identifies these lines along with OH*. To estimate the OPR in comet C/2012 F6, we used eight ortho-water and seven para-water emission lines on February 4 (with CRIRES) and six ortho-water and four para-water emission lines on June 20 (with NIRSPEC). The resulting OPRs (3.78 ± 0.77 with CRIRES and 3.20 ± 0.37 with NIRSPEC) agree within 1σ. Their weighted mean OPR is 3.31 ± 0.33, which constrains the spin temperature to be >37 K at the 95% confidence limit but is consistent with statistical equilibrium. For further details on the significance of OPR measurements, we refer the reader to Mumma & Charnley (2011), Bonev et al. (2013), and references therein.

5. SUMMARY

We investigated the production of primary volatiles in comet C/2012 F6 (Lemmon) using VLT/CRIRES on 2013 February 2 and 4 (pre-perihelion; $R_h = 1.2$ AU), IRTF/CSHELL on March 31 and April 1 (post-perihelion; $R_h = 0.75$ AU), and Keck-2/NIRSPEC on June 20 (post-perihelion; $R_h = 1.74$ AU). We detected 10 volatile species (H_2O, OH* prompt emission, C_2H_6, CH_3OH, H_2CO, HCN, CO, CH_4, NH_3, and NH_2), and obtained upper limits for two others (C_2H_2 and HDO). We quantified the OPR of H_2O using ortho and para emission lines (OPR = 3.31 ± 0.33), which constrains the spin temperature to be >37 K at the 95% confidence limit but is consistent with statistical equilibrium. Our measured production rate for H_2O and upper limit for HDO provided an upper limit for D/H in water ($D/H < 2.45 \times 10^{-3}$, i.e., <16 VSMOW).

With CSHELL we obtained a marginally higher water production rate on April 1 compared with March 31, but the values on both dates showed a reasonable excess compared with CRIRES results in February (and with NIRSPEC results in June), in accord with the increased (decreased) insolation between these epochs.

The obtained volatile abundance ratios are summarized in Table 3. Comet C/2012 F6 is rather depleted in C_2H_6 and CH_3OH; HCN, CH_4, and CO displayed normal abundances, and H_2CO was the only volatile showing an enhancement relative to water. These volatile abundances suggest a certain degree of chemical post-processing and/or formation within warm regions in the nebula. However, the normal abundance of HCN and of the hypervolatiles CH_4 and CO, plus the enhancement

of H_2CO, argues against formation under such conditions, and suggests possible heterogeneity in this comet. Further evidence on this matter will be revealed as additional results from radio, infrared, and optical wavelengths become available.

We thank the VLT science operations team of the European Southern Observatory, Keck Observatory, and NASA's InfraRed Telescope Facility for efficient operations of the observatories. We gratefully acknowledge support by the NASA Postdoctoral Program (Paganini), by NASA's Planetary Astronomy (Paganini, Mumma, DiSanti, Villanueva) and Astrobiology (Mumma, DiSanti, Bonev) Programs, by NSF's Astronomy and Astrophysics Research Grants Program (Bonev), and by the Max Planck Gesellschaft (Böhnhardt). This material is based upon work supported by the National Aeronautics and Space Administration through the NASA Astrobiology Institute under Cooperative Agreement No. NNA09DA77A (Keane, Meech) issued through the Office of Space Science. L.P. also acknowledges Michael R. Combi for fruitful discussions on C/2012 F6 (Lemmon) and for sharing the SWAN results prior to final publication. We also acknowledge Emmanuel Jehin and Cyrielle Opitom for sharing pre-publication results from the TRAPPIST project, and the referee for helpful suggestions. The NASA-IRTF is operated by the University of Hawaii under Cooperative Agreement NCC 5–538 with the NASA-OSS Planetary Astronomy Program. The authors acknowledge the very significant cultural role and reverence that the summit of Mauna Kea has always had within the indigenous Hawaiian community. We are most fortunate to have the opportunity to conduct observations from this mountain.

REFERENCES

A'Hearn, M. F., Feaga, L. M., Keller, H. U., et al. 2012, ApJ, 758, 29
A'Hearn, M. F., Millis, R. L., Schleicher, D. G., Osip, D. J., & Birch, P. V. 1995, Icar, 118, 223
Bockelée-Morvan, D., Biver, N., Swinyard, B., et al. 2012, A&A, 544, L15
Bockelée-Morvan, D., Crovisier, J., Mumma, M. J., & Weaver, H. A. 2004, in Comets II, ed. M. C. Festou, H. U. Keller, & H. A. Weaver (Tucson, AZ: Univ. Arizona Press), 391
Bonev, B. P., Mumma, M. J., DiSanti, M. A., et al. 2006, ApJ, 653, 774
Bonev, B. P., Villanueva, G. L., Paganini, L., et al. 2013, Icar, 222, 740
Brasser, R., & Morbidelli, A. 2013, Icar, 225, 40
Brownlee, D. E., Tsou, P., Aléon, J., et al. 2006, Sci, 314, 1711
Clough, S. A., Shephard, M. W., Mlawer, E. J., et al. 2005, JQSRT, 91, 233
Cochran, A. L., Barker, E. S., & Gray, C. L. 2012, Icar, 218, 144
Combi, M. R., Bertaux, J.-L., Quémerais, E., et al. 2013, EPSC, 8, 794
DiSanti, M. A., Bonev, B. P., Magee-Sauer, K., et al. 2006, ApJ, 650, 470
DiSanti, M. A., Bonev, B. P., Villanueva, G. L., & Mumma, M. J. 2013a, ApJ, 763, 1
DiSanti, M. A., Bonev, B. P., Villanueva, G. L., et al. 2013b, IAUC, 9257
DiSanti, M. A., Dello Russo, N., Magee-Sauer., K., et al. 2002, in Proc. ACM 2002, ed. B. Warmbein (ESA SP-500; Noordwijk: ESA), 571
DiSanti, M. A., Villanueva, G. L., Milam, S. N., et al. 2009, Icar, 203, 589
Dodson-Robinson, S. E., Willacy, K., Bodenheimer, P., Turner, N. J., & Beichman, C. A. 2009, Icar, 200, 672
Fink, U. 2009, Icar, 201, 311
Gibb, E. L., Mumma, M. J., Dello Russo, N., DiSanti, M. A., & Magee-Sauer, K. 2003, Icar, 165, 391
Gomes, R., Levison, H. F., Tsiganis, K., & Morbidelli, A. 2005, Natur, 435, 466
Hartogh, P., Lis, D. C., Bockelée-Morvan, D., et al. 2011, Natur, 478, 218
Jorda, L., Crovisier, J., & Green, D. W. E. 2008, LPICo, 1405, 8046
Kawakita, H., & Mumma, M. J. 2011, ApJ, 727, 91
Langland-Shula, L. E., & Smith, G. H. 2011, Icar, 213, 280
Lippi, M., Villanueva, G. L., DiSanti, M. A., et al. 2013, A&A, 551, A51
Lis, D. C., Biver, N., Bockelée-Morvan, D., et al. 2013, ApJL, 774, L3
Mumma, M. J., Bonev, B. P., Villanueva, G. L., et al. 2011, ApJL, 734, L7
Mumma, M. J., & Charnley, S.B. 2011, ARA&A, 49, 471
Mumma, M. J., DiSanti, M. A., Magee-Sauer, K., et al. 2005, Sci, 310, 270
Nakano, S. 2013, C/2012 F6 (Lemmon), in Nakano Note NK 2558, http://www.oaa.gr.jp/~oaacs/nk/nk2558.htm
Opitom, C., Jehin, E., Manfroid, J., & Gillon, M. 2013a, CBET, 3433
Opitom, C., Jehin, E., Manfroid, J., & Gillon, M. 2013b, CBET, 3530
Paganini, L., Mumma, M. J., Boehnhardt, H., et al. 2013a, ApJ, 766, 100
Paganini, L., Mumma, M. J., Villanueva, G. L., et al. 2012, ApJL, 748, L13
Paganini, L., Mumma, M. J., Villanueva, G. L., et al. 2013b, IAUC, 9255
Qi, C., Öberg, K. I., Wilner, K. I., et al. 2013, Sci, 341, 630
Schleicher, D. G., & Bair, A. N. 2010, BAAS, 42, 945
Tielens, A. G. G. M., & Hagen, W. 1982, A&A, 114, 245
Villanueva, G. L., DiSanti, M. A., Mumma, M. J., & Xu, L.-H. 2012a, ApJ, 747, 37
Villanueva, G. L., Magee-Sauer, K., & Mumma, M. J. 2013, JQSRT, 129, 158
Villanueva, G. L., Mumma, M. J., Bonev, B. P., et al. 2012b, JQSRT, 113, 202
Villanueva, G. L., Mumma, M. J., DiSanti, M. A., et al. 2011a, Icar, 216, 227
Villanueva, G. L., Mumma, M. J., & Magee-Sauer, K. 2011b, JGRE, 116, 08012
Walsh, K. J., Morbidelli, A., Raymond, S. N., O'Brien, D. P., & Mandell, A. M. 2011, Natur, 475, 206
Xie, X., & Mumma, M.J. 1996, ApJ, 464, 457